Supplemental Material

In the Supplementary Information, we show schematic of the non-Hermitian Kapit-Mueller model, numerical evidence of the equality between complex quantum metric and Berry curvature, prove the similarity transformation for relating Hermitian and non-Hermitian Hamiltonian on a cylinder, show analytical wave functions of both single-particle states on the flat band and non-Hermitian Laughlin states, demonstrate the quantum geometry calculated with both left and both right eigenvectors with analytical explanations, show additional details on the single-band projection procedure in the non-Hermitian context and numerical proof, illustrate the emergence of negative energy states and breakdown of variational principle in non-Hermitian systems, briefly introduce the generalized Pauli principle, discuss the stability of the non-Hermitian FCIs within the framework of the Lindblad master equation, and provide more numerical data on spectral flow, entanglement spectrum, signatures of superfluid, many-body energy spectrum beyond the single-band projection and results for $\phi = 1/3$.

I. SCHEMATIC OF THE NON-HERMITIAN KAPIT-MUELLER MODEL.

In this section, we show the schematic of the non-Hermitian KM model, described by Hamiltonian (**??**) in the main text, in Fig. S1. In Hamiltonian (**??**), $J_{ij} = W_{ij} e^{-i\pi y_{ij}(x_i+x_j)\phi}$ with $W_{ij} = (-1)^{x_{ij}+y_{ij}+x_{ij}y_{ij}} e^{-(\pi/2)(1-\phi)(x_{ij}^2+y_{ij}^2)}$, $x_{ij} = x_i - x_j$, and $y_{ij} = y_i - y_j$. Compared to Hofstadter model, the more famous lattice model with flux, the KM model is featured by the long-range hopping, with hoppings within the same row shown in Fig. S1 as examples. The hopping from left to right $J^R_{0n} = e^{\kappa(\pi/2)(1-\phi)n} J_{ij}$ for $x_i - x_j = n, y_i = y_j$ (indicated by blue color) differs from that from right to left $J^L_{0n} = e^{-\kappa(\pi/2)(1-\phi)n} J^*_{ij}$ (indicated by red color) in strength, due to the exponential factor $e^{\pm\kappa(\pi/2)(1-\phi)n}$, leading to the non-Hermiticity.

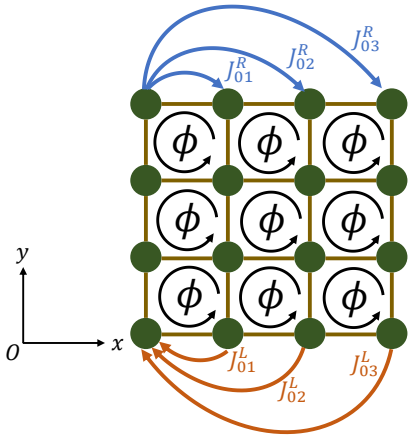

FIG. S1. The flux ϕ in each plaquette is represented by the counterclockwise arrowed circle. The hoppings to the right and left are indicated by blue and red colors, respectively, and the difference between the right and left hoppings leads to the non-Hermiticity.

II. NUMERICAL CONFIRMATION OF IDEAL QUANTUM GEOMETRY

In this section, we justify the ideal quantum geometry numerically by showing the real and imaginary part of $\delta = \mathrm{Tr}(g^{LR}) - \Omega^{LR}_{xy}$ in Fig. S2(a) and (b) with respect to the grid density n_{grid}, i.e., calculated under a $n_{\mathrm{grid}} \times n_{\mathrm{grid}}$ grids in the momentum space. We see δ decreases and tends to zero as n_{grid} increases, indicating the ideal conditions (7) and (8) in the main text are satisfied.

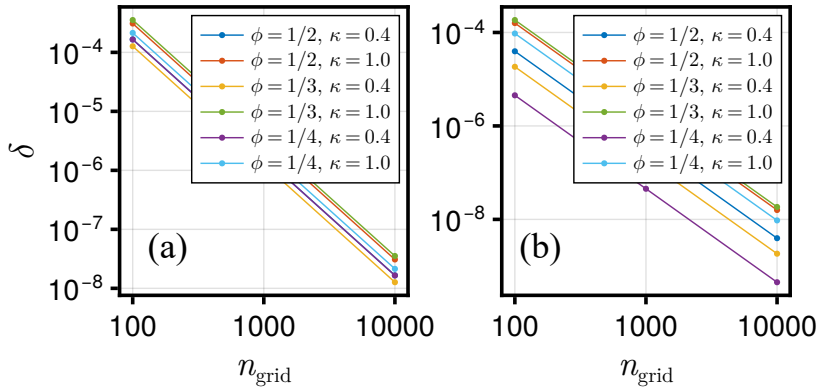

FIG. S2. Difference of the (a)Real and (b) imaginary part between quantum metric g^{LR} and Berry curvature Ω_{xy}^{LR} versus the grid density n_{grid}.

III. SIMILARITY TRANSFORMATION FOR NON-HERMITIAN SKIN EFFECT

In this section, we prove both the single-particle and many-body Hamiltonian under non-Hermitian deformation in the main text can be related to their Hermitian counterparts by a similarity transformation on a cylinder, from which the non-Hermitian skin effect is clear. We take the second quantization formulation in the proof.

The single-particle Hamiltonian of the Kapit-Mueller (KM) model in Eq.1 of the main text reads

$$H_0(\kappa) = \sum_{i \neq j} e^{-\gamma(x_j - x_i)} J_{ij} a_i^\dagger a_j, \tag{S1}$$

where we denote $\gamma = \kappa(\pi/2)(1-\phi)$ for simplicity. The similarity transformation operator is $S(\kappa) = e^{\gamma \sum_i x_i a_i^\dagger a_i} = e^{\gamma \sum_i x_i n_i}$ with $n_j = a_j^\dagger a_j$ being the particle number operator. As the number operators commute with each other, we have $S^{-1}(\kappa) = e^{-\gamma \sum_i x_i n_i}$. In the following, we prove the relation

$$H_0(\kappa) = S(\kappa) H_0(0) S^{-1}(\kappa) \tag{S2}$$

independent of whether $a_i^\dagger$ (a_i) is the creation (annihilation) operator of bosons or fermions. The most important tool in the proof is the Baker-Campbell-Hausdorff (BCH) formula

$$e^A B e^{-A} = B + [A,B] + \frac{1}{2!}[A,[A,B]] + ... + \frac{1}{n!}[A,[A,...[A,B]]] \tag{S3}$$

where A, B are operators, $[...]$ denotes the commutator and n is an integer tending to infinity. Using the BCH formula, we can directly obtain

$$S(\kappa) a_i^\dagger a_j S^{-1}(\kappa) = a_i^\dagger a_j + \gamma(x_i - x_j) a_i^\dagger a_j + \frac{1}{2!}[\gamma(x_i - x_j)]^2 a_i^\dagger a_j + ... + \frac{1}{n!}[\gamma(x_i - x_j)]^n a_i^\dagger a_j \tag{S4}$$

$$= e^{\gamma(x_i - x_j)} a_i^\dagger a_j, \tag{S5}$$

where we have used the equation $[\sum_m x_m a_m^\dagger a_m, a_i^\dagger a_j] = (x_i - x_j) a_i^\dagger a_j$, which can be proved easily for both bosons and fermions. Therefore, the single-particle case Eq. S2 is proved.

The many-body Hamiltonian for interacting bosons in Eq. 9 in the main text is $H(\kappa) = H_0(\kappa) + H_I$ with

$$H_I = \sum_j \frac{U}{2} a_j^\dagger a_j^\dagger a_j a_j = \sum_j \frac{U}{2} n_j (n_j - 1) \tag{S6}$$

As number operators commute, it is obvious that H_I is invariant under the similarity transformation by S also from BCH formula. Combining Eq. S2, we arrive at $H(\kappa) = S(\kappa) H(0) S^{-1}(\kappa)$ for the total Hamiltonian of interacting bosons. Therefore, the right and left eigenvectors $|\Psi^R(\kappa)\rangle$ and $|\Psi^L(\kappa)\rangle$ of $H(\kappa)$ are related to the eigenstate $|\Psi\rangle$ of the Hermitian Hamiltonian $H(0)$ by

$$|\Psi^R(\kappa)\rangle = S(\kappa)|\Psi\rangle, \tag{S7}$$

$$\langle\Psi^L(\kappa)| = \langle\Psi| S^{-1}(\kappa), \tag{S8}$$

leading to the non-Hermitian skin effect.

By the similarity transformation, we can prove on the cylinder the biorthogonal number density defined in the main text

$$\rho_b(i) = \langle \Psi^L(\kappa)|a_i^\dagger a_i|\Psi^R(\kappa)\rangle \tag{S9}$$

$$= \langle \Psi|S^{-1}(\kappa)a_i^\dagger a_i S(\kappa)|\Psi\rangle \tag{S10}$$

$$= \langle \Psi|a_i^\dagger a_i|\Psi\rangle, \tag{S11}$$

which is identical to the particle number density of the Hermitian state $|\Psi\rangle$. In the proof, we have used the commutating relation $[S(\kappa), a_i^\dagger a_i] = 0$.

IV. ANALYTICAL WAVE FUNCTIONS ON THE TORUS

In this section, we give analytical wave functions on the torus for both the flat band of the non-Hermitian KM model at the single-particle level and the non-Hermitian FCI states in the interacting regime.

First, we review the standard textbook problem of a charged particle under a magnetic field with strength B corresponding to the vector potential $\boldsymbol{A} = (A_x, A_y, 0)$ in the continuum with Hamiltonian

$$H_{con} = \frac{1}{2m}[\pi_x^2 + \pi_y^2], \tag{S12}$$

where q, m are electric charge and mass of the particle, respectively, and $\pi_\mu = -i\hbar\partial_\mu - qA_\mu$ with $\mu = x, y$ and $\hbar$ being the Planck constant. By defining ladder operators

$$a = \frac{l_B}{\sqrt{2}\hbar}\Big(i\pi_x - \pi_y\Big), \tag{S13}$$

$$a^\dagger = \frac{l_B}{\sqrt{2}\hbar}\Big(-i\pi_x - \pi_y\Big), \tag{S14}$$

with magnetic length $l_B = \sqrt{\hbar/(qB)}$, we arrive at

$$H_{con} = \hbar\omega(a^\dagger a + \frac{1}{2}) \tag{S15}$$

with $\omega = qB/m$. As eigenvalues of $a^\dagger a$ take non-negative integer values, the Hamiltonian (S15) yields Landau level energy spectrum $E_{LL} = \hbar\omega/2, 3\hbar\omega/2, 5\hbar\omega/2, ...$ The wave functions on the lowest Landau level satisfy $a\psi(x, y) = 0$. If we choose the symmetric gauge $\boldsymbol{A} = (By/2, -Bx/2, 0)$ for the convenience in constructing Laughlin wave functions in the following, we have

$$a = \frac{1}{\sqrt{2}}\left(2l_B\partial_{\bar{z}} + \frac{z}{2l_B}\right) \tag{S16}$$

$$a^\dagger = \frac{1}{\sqrt{2}}\Big(-2l_B\partial_z + \frac{\bar{z}}{2l_B}\Big). \tag{S17}$$

For a system with lengths L_1, L_2 along two directions separated by an angle θ, i.e., $\boldsymbol{L}_1 = (L_1, 0), \boldsymbol{L}_2 = (L_2\cos\theta, L_2\sin\theta)$ the wave function under PBCs has the form [1]

$$\psi(z) = e^{(z^2 - |z|^2)/(4l_B^2)}\prod_{\nu=1}^{N_\phi}\theta_1(\pi(z - z_\nu)/L_1|\tau) \tag{S18}$$

where the odd elliptic theta function $\theta_1(z|\tau) = \sum_{n=-\infty}^{\infty}(-1)^{n+1/2}e^{i\pi\tau(n+1/2)^2}e^{i2z(n+1/2)}$ with $\tau = e^{i\theta}L_2/L_1$, N_ϕ is the degeneracy of the Landau level and z_ν are parameters adequately chosen to satisfy the specific boundary conditions under magnetic translations. Explicitly,

$$\psi(z + L_1) = (-1)^{N_\phi}\exp\Big(iL_1y/(2l_B^2)\Big)\psi(z), \tag{S19}$$

$$\psi(z + e^{i\theta}L_2) = (-1)^{N_\phi}\exp\Big(-L_2(e^{i\theta}z^* - e^{-i\theta}z)/(2l_B^2)\Big)\exp\left[i2\pi\frac{\sum_v z_\nu}{L_1}\right]\psi(z). \tag{S20}$$

If N_ϕ is even, the magneto-periodic boundary conditions constrain $\sum_v z_\nu = nL_1$ with integer n.

By introducing the imaginary gauge potential $\boldsymbol{A}_{imag} = (i\gamma, 0, 0)$, we obtain the non-Hermitian Hamiltonian

$$H_{con}^{NH} = \frac{1}{2m}[(\pi_x - iq\gamma)^2 + \pi_y^2], \tag{S21}$$

which can be rewritten as

$$H_{con}^{NH} = \hbar\omega(b^+ b + \frac{1}{2}), \tag{S22}$$

with

$$b = a + \frac{el_B}{\sqrt{2}\hbar}\gamma, \tag{S23}$$

$$b^+ = a^\dagger - \frac{el_B}{\sqrt{2}\hbar}\gamma, \tag{S24}$$

where we use $+$ instead of $\dagger$ to indicate b^+ and b are not Hermitian conjugate of each other. The derivation of (S22) is independent of the boundary conditions, therefore the Landau level spectrum does not change under the non-Hermitian deformation even on the torus. Under the symmetric gauge, it is easy to see

$$b = \frac{1}{\sqrt{2}}\left(2l_B\partial_{\bar{z}^R} + \frac{z^R}{2l_B}\right), \tag{S25}$$

$$b^+ = \frac{1}{\sqrt{2}}\left(-2l_B\partial_{z^L} + \frac{\bar{z}^L}{2l_B}\right) \tag{S26}$$

with $z^R = z + 2ql_B^2\gamma/\hbar, z^L = z - 2ql_B^2\gamma/\hbar$. Due to $b\psi^R(z) = 0$ and $(b^+)^\dagger\psi^L(z) = 0$, we arrive at the right and left eigenvectors under the imaginary gauge potential:

$$\psi^R(z) = e^{((z^R)^2 - |z^R|^2)/(4l_B^2)}\prod_{\nu=1}^{N_\phi}\theta_1(\pi(z^R - \tilde{z}_\nu^R)/L_1|\tau), \tag{S27}$$

$$\psi^L(z) = e^{((z^L)^2 - |z^L|^2)/(4l_B^2)}\prod_{\nu=1}^{N_\phi}\theta_1(\pi(z^L - \tilde{z}_\nu^L)/L_1|\tau), \tag{S28}$$

which are opposite spatial shifts along x direction. It is easy to see $\psi^X(z)$ with $X = R, L$ satisfies Eq. S19 while an extra phase factor $e^{\mp iq\gamma L_y/\hbar}$ arises, so to preserve the boundary conditions, we have $\sum_\nu \tilde{z}_\nu^R - \sum_\nu z_\nu = q\gamma L_1 L_2/(2\pi\hbar)$ and $\sum_\nu \tilde{z}_\nu^L - \sum_\nu z_\nu = -q\gamma L_1 L_2/(2\pi\hbar)$.

On the original KM model, the wave function on the flat band is the lattice discretization of the lowest Landau level wave function in the continuum [2] by substituting $1/l_B^2$ with $2\pi\phi$. It is also the case under the imaginary gauge potential, i.e., the wave functions read

$$\psi_{KM}^R(z) = e^{((z^R)^2 - |z^R|^2)\pi\phi/2}\prod_{\nu=1}^{N_\phi}\theta_1(\pi(z^R - \tilde{z}_\nu^R)/L_1|\tau), \tag{S29}$$

$$\psi_{KM}^L(z) = e^{((z^L)^2 - |z^L|^2)\pi\phi/2}\prod_{\nu=1}^{N_\phi}\theta_1(\pi(z^L - \tilde{z}_\nu^L)/L_1|\tau), \tag{S30}$$

on the non-Hermitian KM model, where $z^R = z + \gamma/(\pi\phi), z^L = z - \gamma/(\pi\phi)$ corresponding to $\boldsymbol{A}_{imag} = (i\gamma, 0, 0)$, and $\sum_\nu \tilde{z}_\nu^R - \sum_\nu z_\nu = L_1 L_2\gamma/(2\pi), \sum_\nu \tilde{z}_\nu^L - \sum_\nu z_\nu = -L_1 L_2\gamma/(2\pi)$ to keep the boundary conditions intact. In the following, we will prove mathematically.

We reproduce the Hamiltonian of the non-Hermitian KM model on a torus here:

$$H_0(\gamma) = \sum_{j,k,R}^{z_j \neq z_k + R}\Gamma(z_j, z_k + R, \gamma)J(z_j, z_k + R)P(z_k, R)a_j^\dagger a_k, \tag{S31}$$

where $R = nL_x + me^{i\theta}L_y$ with integer n, m. For the lattice model, we consider the case with $\theta = \pi/2$ for simplicity, so we use L_x, L_y instead of L_1, L_2 afterwards. Here, $\Gamma(z_j, z_k, \gamma) = e^{\gamma(z_{kj}+z^*_{kj})/2}$ with $z_{kj} = z_k - z_j$ being the non-reciprocal hopping, $J(z_j, z_k) = (-1)^{x_{jk}+y_{jk}+x_{jk}y_{jk}} e^{-(\pi/2)[(1-\phi)|z|^2]} e^{(\pi/2)(z_j z^* - z_j^* z)\phi}$ with $x_{kj} = x_k - x_j, y_{kj} = y_k - y_j$ is the hopping term of the pristine KM model, and $P(z_k, R) = e^{\pi\phi(z_k R^* - z_k^* R)/2}$ is the extra phase for hopping across the boundaries, where $z = x + iy$ and $u_{kj} = u_k - u_j$ for $u = z, x, y$. From Eq. S19 and S20, we have

$$\psi^R(z + R) = P(z, R)\psi^R(z) \tag{S32}$$

if we choose N_ϕ is even and $\sum_\nu z_\nu$ is an integer multiple of L_x. Then we have

$$\frac{\langle j|H_0(\gamma)|\psi^R\rangle}{\langle j|\psi^R\rangle} = \frac{\sum_{k,R}^{z_j\neq z_k+R} \Gamma(z_j, z_k + R, \gamma) J(z_j, z_k + R) P(z_k, R)\psi^R(z_k + \frac{\gamma}{\pi\phi})}{\psi^R(z_j)} \tag{S33}$$

$$= \frac{\sum_{k,R}^{z_j\neq z_k+R} \Gamma(z_j, z_k + R, \gamma) J(z_j, z_k + R) P(z_k, R) P^{-1}(z_k, R)\psi^R(z_k + \frac{\gamma}{\pi\phi} + R)}{\psi^R(z_j)} \tag{S34}$$

$$= \sum_{k,R}^{z_j\neq z_k+R} \prod_{\nu=1}^{N_\phi} \frac{\exp\left(\frac{\pi\phi}{2}(z_j + z_{jk} + \frac{\gamma}{\pi\phi} + R)^2\right)\theta_1[\pi(z_j + z_{jk} + \frac{\gamma}{\pi\phi} + R - \tilde{z}^R_\nu)/L_x|\tau]}{\exp\left(\frac{\pi\phi}{2}\left(z_j + \frac{\gamma}{\pi\phi}\right)^2\right)\theta_1[\pi(z_j + \frac{\gamma}{\pi\phi} - \tilde{z}^R_\nu)/L_x|\tau]}$$

$$\exp\Big(-\pi\phi z_j^*(z_{jk} + R)\Big) G(z_{jk} + R) \exp\Big(-\frac{\pi}{2}|z_{jk} + R|^2\Big). \tag{S35}$$

Due to the relation $\sum_z f(z)G(z)e^{-(\pi/2)|z|^2} = 0$ for any entire function $f(z)$, we have $\langle j|H_0(\gamma)|\psi^R\rangle/\langle j|\psi^R\rangle = -1$ because the summation in Eq. S35 discards $z_{jk} + R = 0$. Similarly, we can also prove $\langle j|H_0^\dagger(\gamma)|\psi^L\rangle/\langle j|\psi^L\rangle = -1$. Therefore, we have proved Eq. S29 and S30 are eigen wave functions of the non-Hermitian KM model at energy -1, which also explains the persistence of the flat band under non-Hermitian deformation.

The Laughlin wave function at filling factor $\nu = 1/p$ for the Hermitian KM model on a torus is [2]

$$\Psi(z_n) = \prod_{i=1}^{p} \theta_1\left(\frac{\pi}{L}(Z - Z_i)\Big|\tau\right) \prod_{k<j}^{N} \theta_1\left(\frac{\pi}{L}(z_j - z_k)\Big|\tau\right)^p \prod_{j=1}^{N} e^{(z_j^2 - |z_j|^2)\pi\phi/2}, \tag{S36}$$

where N is the number of particles, $Z = \sum_j z_j$ is the center of mass coordinate and Z_i are parameters. From Eq.(S29) and (S30), we deduce the right and left eigenvectors of the zero modes on the non-Hermitian KM model under onsite interaction are

$$\Psi^R(z_n, \kappa) = \prod_{i=1}^{p} \theta_1\left(\frac{\pi}{L}(Z^R - \tilde{Z}^R_i)\Big|\tau\right) \prod_{k<j}^{N} \theta_1\left(\frac{\pi}{L}(z_j - z_k)\Big|\tau\right)^p \prod_{j=1}^{N} e^{((z_j^R)^2 - |z_j^R|^2)\pi\phi/2}, \tag{S37}$$

$$\Psi^L(z_n, \kappa) = \prod_{i=1}^{p} \theta_1\left(\frac{\pi}{L}(Z^L - \tilde{Z}^L_i)\Big|\tau\right) \prod_{k<j}^{N} \theta_1\left(\frac{\pi}{L}(z_j - z_k)\Big|\tau\right)^p \prod_{j=1}^{N} e^{((z_j^L)^2 - |z_j^L|^2)\pi\phi/2} \tag{S38}$$

with $\sum_i \tilde{Z}^R_i - \sum_i Z_i = L_x L_y \gamma/(2\pi), \sum_i \tilde{Z}^L_i - \sum_i Z_i = -L_x L_y \gamma/(2\pi)$ to satisfy the original boundary conditions. which we have numerically confirmed.

V. QUANTUM GEOMETRY CALCULATED WITH RIGHT-RIGHT OR LEFT-LEFT EIGENVECTORS

In this section, we show the quantum geometry of the non-Hermitian ideal Chern band calculated with solely right or left eigenvectors and provide analytical explanations.

We numerically find both $g^{XX}_{\mu\nu}$ and $\Omega^{XX}_{\mu\nu}$ defined in Eq. (5) and (6) in the main text are purely real for $X = R$ and $X = L$. The ideal trace condition is satisfied, i.e.,

$$\mathrm{Tr}(g^{XX}) = \Omega^{XX}_{xy}. \tag{S39}$$

In Fig. S3, we show $\mathrm{Tr}(g^{RR})$ [$\mathrm{Tr}(g^{LL})$] equal to Ω^{RR}_{xy} (Ω^{LL}_{xy}) in the upper (lower) row for $\kappa = 0.0, 0.5, 1.0$, respectively, from left to right. We see the non-Hermitian deformation induces a shift of the quantum geometry pattern along positive (negative) direction along k_y, which we will explain analytically in the following.

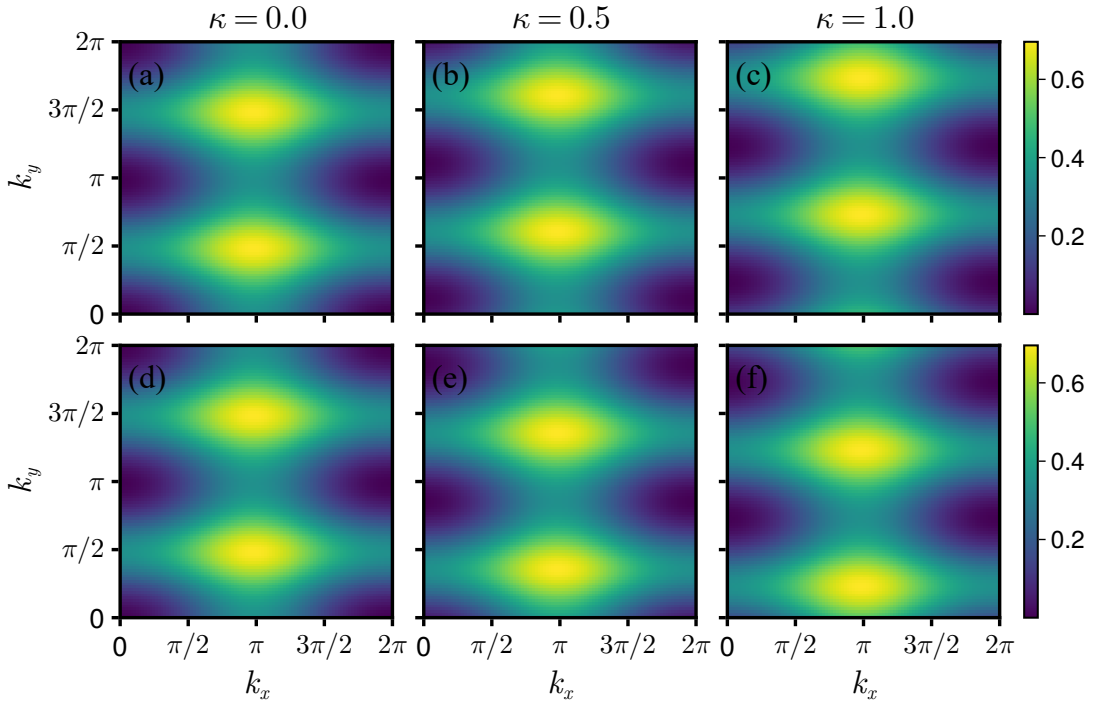

FIG. S3. $\mathrm{Tr}(g^{RR})(=\Omega_{xy}^{RR})$ (upper row) and $\mathrm{Tr}(g^{LL})(=\Omega_{xy}^{LL})$ (lower row) for (a)(d) $\kappa = 0$, (b)(e) $\kappa = 0.5$ and (c)(f) $\kappa = 1.0$.

Again, we start from the continuum problem as in Sec.IV. For consistency with the numerical results, we use the Landau gauge $\boldsymbol{A} = (0, Bx, 0)$ and obtain ladder operators

$$a = \frac{l_B}{\sqrt{2}\hbar}\Big(\hbar\partial_x - i\hbar\partial_y - qBx\Big), \tag{S40}$$

$$a^\dagger = \frac{l_B}{\sqrt{2}\hbar}\Big(-\hbar\partial_x - i\hbar\partial_y - qBx\Big) \tag{S41}$$

for Eq. S15. In the momentum space, the ladder operators take the form of

$$a = \frac{l_B}{\sqrt{2}\hbar}\Big(i\hbar k_x + \hbar k_y + iqB\partial_{k_x}\Big), \tag{S42}$$

$$a^\dagger = \frac{l_B}{\sqrt{2}\hbar}\Big(-i\hbar k_x + \hbar k_y + iqB\partial_{k_x}\Big). \tag{S43}$$

From Eq. S23 and S24, we obtain

$$b = \frac{l_B}{\sqrt{2}\hbar}\Big(i\hbar k_x + \hbar k_y^R + iqB\partial_{k_x}\Big), \tag{S44}$$

$$b^+ = \frac{l_B}{\sqrt{2}\hbar}\Big(-i\hbar k_x + \hbar k_y^L + iqB\partial_{k_x}\Big) \tag{S45}$$

where $k_y^R = k_y + q\gamma/\hbar, k_y^L = k_y - q\gamma/\hbar$. Therefore, following the similar reasoning in Sec. IV, the right and left eigenvectors on the lowest Landau level are $\psi^R(k_x, k_y) = \psi(k_x, k_y + q\gamma/\hbar), \psi^L(k_x, k_y) = \psi(k_x, k_y - q\gamma/\hbar)$ with $\psi(k_x, k_y)$ being the Hermitian Landau level wave function. Utilizing the mapping between lowest Landau level wave functions in the continuum and flat band in the KM model even in the non-Hermitian regime proved in Sec. IV, we arrive at $\psi_{KM}^R(k_x, k_y) = \psi_{KM}(k_x, k_y + \kappa(\pi/2)(1-\phi)), \psi_{KM}^L(k_x, k_y) = \psi_{KM}(k_x, k_y - \kappa(\pi/2)(1-\phi))$ for the lattice wave functions on the flat band, which explains the spatial shift of the quantum geometry pattern in Fig. S3 under the non-Hermitian deformation.

VI. SINGLE-BAND PROJECTION IN THE NON-HERMITIAN CONTEXT

In this section, we provide details of the single-band projection in the non-Hermitian context and show the validity of this approximation numerically.

For generality, we consider a general free-particle Hamiltonian with translational invariance

$$H_f = \sum_{k,\alpha,\beta} a^\dagger_{k,\alpha} H_f^{\alpha,\beta}(k) a_{k,\beta}, \tag{S46}$$

where k is the index of the lattice momentum, α, β are internal degrees of freedom within a unit cell and $H_f^{\alpha,\beta}(k)$ is the matrix element of the first-quantized Hamiltonian $H_f(k)$. For a non-Hermitian system, $H_f(k)$ is a non-Hermitian matrix which can be diagonalized as

$$H_f(k) = \sum_{n,k} \epsilon_{n,k} |u_n^R(k)\rangle\langle u_n^L(k)|, \tag{S47}$$

where $\epsilon_{n,k}$ is the eigenenergy of band n and $|u_n^R(k)\rangle$ and $|u_n^L(k)\rangle$ are the corresponding right and left eigenvectors satisfying $\langle u_n^L(k)|u_m^R(k)\rangle = \delta_{nm}$. The second quantized Hamiltonian Eq. S46 can be written as

$$H_f = \sum_{n,k} \epsilon_{n,k} c^+_{n,k} c_{n,k}, \tag{S48}$$

where

$$c^+_{n,k} = \sum_\alpha [u_n^R(k)]_\alpha a^\dagger_{k,\alpha}, \tag{S49}$$

$$c_{n,k} = \sum_\alpha [u_n^L(k)]^*_\alpha a_{k,\alpha}, \tag{S50}$$

with $[u_n^R(k)]_\alpha$ ($[u_n^L(k)]_\alpha$) being the amplitude of the wave function $|u_n^R(k)\rangle$ ($|u_n^L(k)\rangle$) on the internal orbital α. Due to the biorthonormalization relation $\langle u_n^L(k)|u_m^R(k)\rangle = \delta_{nm}$, $c_{n,k}$ and $c^+_{n,k}$ keep the original statistics of $a_{k,\beta}$ and $a^\dagger_{k,\alpha}$, i.e., for bosons satisfying the commuting relations $[c_{n_1,k_1}, c_{n_2,k_2}] = 0, [c^+_{n_1,k_1}, c^+_{n_2,k_2}] = 0, [c_{n_1,k_1}, c^+_{n_2,k_2}] = \delta_{n_1 n_2}\delta_{k_1 k_2}$ and for fermions satisfying the anti-commuting relations $\{c_{n_1,k_1}, c_{n_2,k_2}\} = 0, \{c^+_{n_1,k_1}, c^+_{n_2,k_2}\} = 0, \{c_{n_1,k_1}, c^+_{n_2,k_2}\} = \delta_{n_1 n_2}\delta_{k_1 k_2}$. However, $c_{n,k}$ and $c^+_{n,k}$ are not Hermitian conjugate of each other, thus we use + instead of †. Therefore, $c_{n,k}$ and $c^+_{n,k}$ can be viewed as non-Hermitian generalization of creation and annihilation operators.

Eq. S49 and S50 represent a similarity transformation because of the biorthonormalization relation. Therefore we can get the inverse transformation

$$a^\dagger_{k,\alpha} = \sum_n [u_n^L(k)]^*_\alpha c^+_{n,k}, \tag{S51}$$

$$a_{k,\alpha} = \sum_n [u_n^R(k)]_\alpha c_{n,k}. \tag{S52}$$

Then for a general interaction in momentum space

$$V_I = \sum_{k_1,\alpha_1,k_2,\alpha_2,k_3,\alpha_3,k_4,\alpha_4} U(k_1,\alpha_1,k_2,\alpha_2,k_3,\alpha_3,k_4,\alpha_4) a^\dagger_{k_1,\alpha_1} a^\dagger_{k_2,\alpha_2} a_{k_3,\alpha_3} a_{k_4,\alpha_4} \tag{S53}$$

$$= \sum_{k_1,n_1,k_2,n_2,k_3,n_3,k_4,n_4} \tilde{U}(k_1,n_1,k_2,n_2,k_3,n_3,k_4,n_4) c^+_{n_1,k_1} c^+_{n_2,k_2} c_{n_3,k_3} c_{n_4,k_4}, \tag{S54}$$

where

$$\tilde{U}(k_1,n_1,k_2,n_2,k_3,n_3,k_4,n_4) = \sum_{\alpha_1,\alpha_2,\alpha_3,\alpha_4} U(k_1,\alpha_1,k_2,\alpha_2,k_3,\alpha_3,k_4,\alpha_4) [u^L_{n_1}(k_1)]^*_{\alpha_1} [u^L_{n_2}(k_2)]^*_{\alpha_2} [u^R_{n_3}(k_3)]_{\alpha_3} [u^R_{n_4}(k_4)]_{\alpha_4}. \tag{S55}$$

Numerically, we can diagonalize V_I in the Fock basis associated with $c_{n,k}$ and $c^+_{n,k}$ like in the conventional Hermitian Fock basis (actually biorthogonal Fock basis here). If we focus on a single band indexed by n_0 and assume the effect from other bands is negligible, we arrive at

$$V_I \approx \sum_{k_1,k_2,k_3,k_4} \tilde{U}(k_1, n_0, k_2, n_0, k_3, n_0, k_4, n_0) c^+_{n_0,k_1} c^+_{n_0,k_2} c_{n_0,k_3} c_{n_0,k_4}. \tag{S56}$$

To validate the single-band projection for non-Hermitian systems, we calculate the many-body spectrum of Eq. 9 in the main text both with and without the projection, as shown in Fig. S4. Fig. S4(a) and (b) shows the real part of the energy spectrum at $\kappa = 0.5$, at which zero modes are ground states, and (a) is calculated under single-band projection and (b) without projection at interaction strength $U = 0.001$. We see the energy spectrum in (a) and (b) are the same. Note that for (b) the kinetic energy $E_{kin} = n_b E_{flat}$ has been subtracted with n_b being the particle number and $E_{flat} = -1$ the single-particle energy of the flat band, and the energy has been normalized to the same scale as (a) where the interaction strength is the only energy scale and chosen arbitrarily. Similarly, Fig. S4(c) and (d) are also the same for $\kappa = 0.7$, after the zero modes transition out of the ground state sector. Therefore, we show the validity of the single-band projection in the non-Hermitian context.

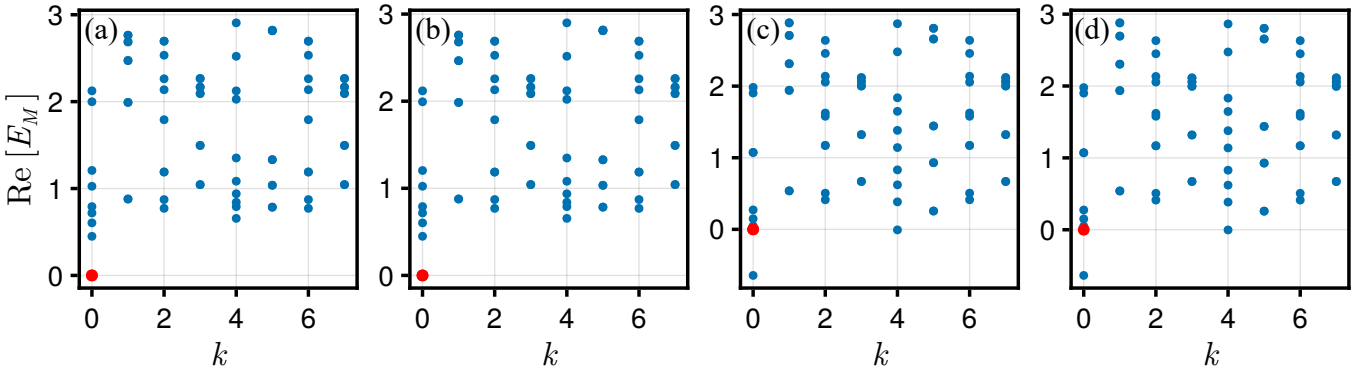

FIG. S4. Real part of the many-body energy spectrum with and without the single-band projection for system size $L_x = 4, L_y = 4$ and flux $\phi = 1/2$. (a) With single-band projection at $\kappa = 0.5$. (b) Without single-band projection at $\kappa = 0.5$ and $U = 0.001$. (c) With single-band projection at $\kappa = 0.7$. (d) Without single-band projection at $\kappa = 0.7$ and $U = 0.001$. For (b) and (d), the single-particle energy has been subtracted and the energy has been renormalized to the same scale as (a) and (c).

VII. SPECTRAL FLOW

In this section, we exhibit the spectral flow to show the existence of a finite gap in the regime with fractional Chern insulators (FCIs) as ground states, and the gapless nature of the system after FCIs transition out of the ground state sector.

In Fig. S5, We show the spectral flow under twisted boundary phase Φ_x (Φ_y) along x (y) direction. We show the spectral flow at $\kappa = 0.6$ about Φ_x and Φ_y in Fig. S5(a) and (b), respectively, where we see a persistent finite gap between the FCIs (indicated by red color) and excited states. At $\kappa = 0.67$, close to the transition point, as shown in Fig. S5(c), we see the single state with negative energy under no twisted boundary phase can float above zero energy during the spectral flow and become indistinguishable from the dense excited states at some points, implying the system is gapless. When we further increase κ to 0.9, as shown in Fig. S5(d), more states drop below zero energy and we cannot identify an isolated manifold of states in the spectral flow pattern, further indicating the gapless nature of the system.

VIII. ENERGY SPECTRUM IN THE COMPLEX ENERGY PLANE AND UNDER COMPLEX INTERACTION U

In this section, we exhibit the many-body energy spectrum in the complex energy plane and demonstrate that the FCIs can be engineered as the longest-lived states by complex interaction strength U.

For the interacting non-Hermitian KM model in the topologically ordered regime, at real U under single-band projection, the FCIs are steady states as the energy is purely real, as indicated by red color in Fig. S6(a). On the

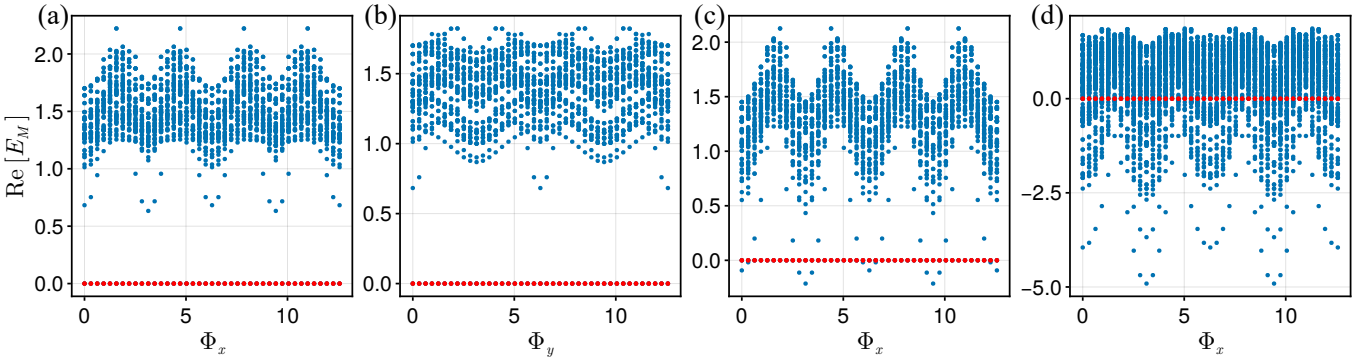

FIG. S5. (a)-(b) Spectral flow at $\kappa = 0.6$ about (a) Φ_x and (b) Φ_y. (a)-(b) Spectral flow about Φ_x at (c) $\kappa = 0.67$ and (d) $\kappa = 0.9$. The system size is $L_x = 6, L_y = 4$ and flux is $\phi = 1/2$.

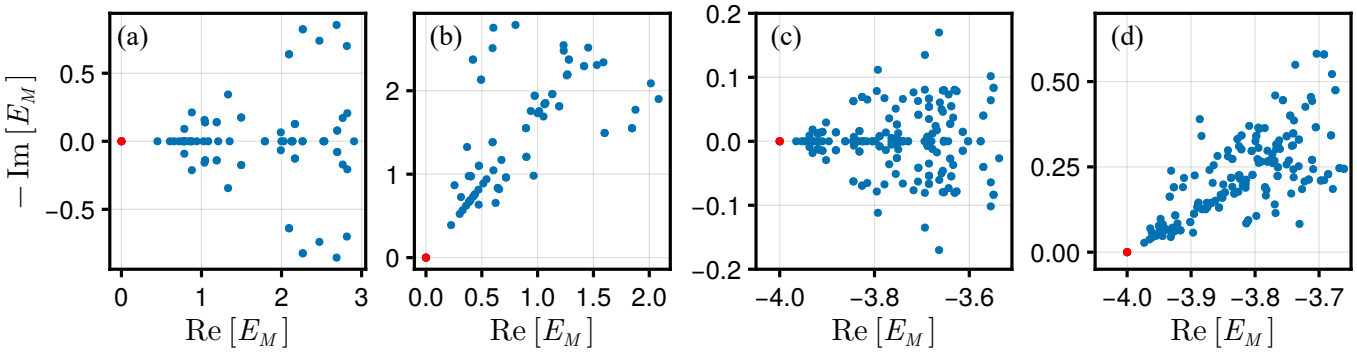

FIG. S6. Many-body energy spectrum in the complex plane for $\kappa = 0.5, L_x = L_y = 4, n_b = 4, \phi = 1/2$. The energies are calculated under single-band projection with $|U| = 1$ for (a),(b) while without the projection with $|U| = 0.1$ for (c),(d). For (a),(c), U is real, i.e., $\theta = 0$ while for (b),(d), $\theta = -\pi/3$.

other hand, the energy spectrum is symmetric about the real axis, indicating excited states with positive Im $[E_M]$ will amplify with time. If we choose complex $U = |U|e^{i\theta}$, which can be realized by particle loss in realistic experiments [3], the energy spectrum is rotated by θ in the complex energy plane about $E_M = 0$, the energy of the FCIs. Therefore, as long as the pattern of the complex energy spectrum can be enveloped within an acute angle with vertex at $E_M = 0$, there always exists a range of θ such that all the excited states have positive real part and negative imaginary part of the energy, as shown in Fig. S6(b). In other words, the FCIs have the longest lifetime, justifying the possible experimental realization in principle. Without the single-band projection, the result still holds, as shown in Fig. S6(c) and (d).

IX. GENERALIZED PAULI PRINCIPLE

The degeneracy of the FCIs and corresponding momentum sectors can be predicted by the generalized principle [4, 5], which we explain here for $\nu = 1/p = n_b/N$ bosonic Laughlin states with even p. We rearrange the N single-particle orbitals into a one-dimensional chain, and load n_b particles into the orbitals. For $\nu = 1/p$ bosonic Laughlin states, permissible configurations (called root configurations in Ref. 5) satisfy the condition that, there exist at most one particle in every p consecutive orbitals. For $p = 2$, there are two permissible configurations, 101010... and 010101..., yielding two-fold degeneracy of FCIs, and the sums of the momenta of occupied orbitals in the configurations predict the associated momentum sectors. If the degeneracy and momentum sectors obtained by numerics coincide with the predictions of the generalized Pauli principle, it suggests the existence of FCIs.

For the particle entanglement spectrum, we partition the total n_b bosons into A and B parts with n_A and n_B particles, respectively, and trace out the B part, arriving at a reduced density matrix $\rho_A = \mathrm{Tr}_B(\sum_i |\Psi_i^X\rangle\langle\Psi_i^{X'}|/2)$ where the summation is over all the zero modes and $X = L/R$ represents left/right eigenvectors. The eigenvalues of ρ_A are $e^{-\xi}$ where ξ is the particle entanglement spectrum. There is a gap in the particle entanglement spectrum of FCIs, under which the number of states can also be predicted by the generalized Pauli principle for $\nu = 1/p$

bosonic Laughlin states. We load n_A particles into the N orbitals rearranged into one dimension, and the number of permissible configurations–at most one particle in every p consecutive orbitals–is equivalent to the number of states under the gap in the particle entanglement spectrum. The consistency between the numbers of states obtained numerically and theoretically is a further confirmation of FCIs.

X. ENTANGLEMENT SPECTRUM

In this section, we show more data on the entanglement spectrum to confirm the zero modes are FCIs.

We calculate the entanglement spectrum using the right eigenvectors of the zero modes, i.e., $X = X' = R$ for $\rho_A = \mathrm{Tr}_B(\sum_i |\Psi_i^X\rangle\langle\Psi_i^{X'}|/2)$, for system size $L_x = 6, L_y = 4$ as shown in Fig. S7. We show results for the Hermitian case ($\kappa = 0$) in the left column, the non-Hermitian FCI phase ($\kappa = 0.6$) in the middle column and the phase with negative energy ($\kappa = 0.8$) in the right column. In all the subfigures, we see a large gap indicated by the red dashed line. The number of states below the gap is 54 for the first row with $n_A = 2$ and 112 for the second row with $n_A = 3$, consistent with the generalized Pauli principle. Therefore, the entanglement spectrum verifies that the exact zero modes are FCIs, even in the presence of negative energy states. Note that ξ of the states above the gap is infinite in principle and arises at finite value in our plot due to the machine precision.

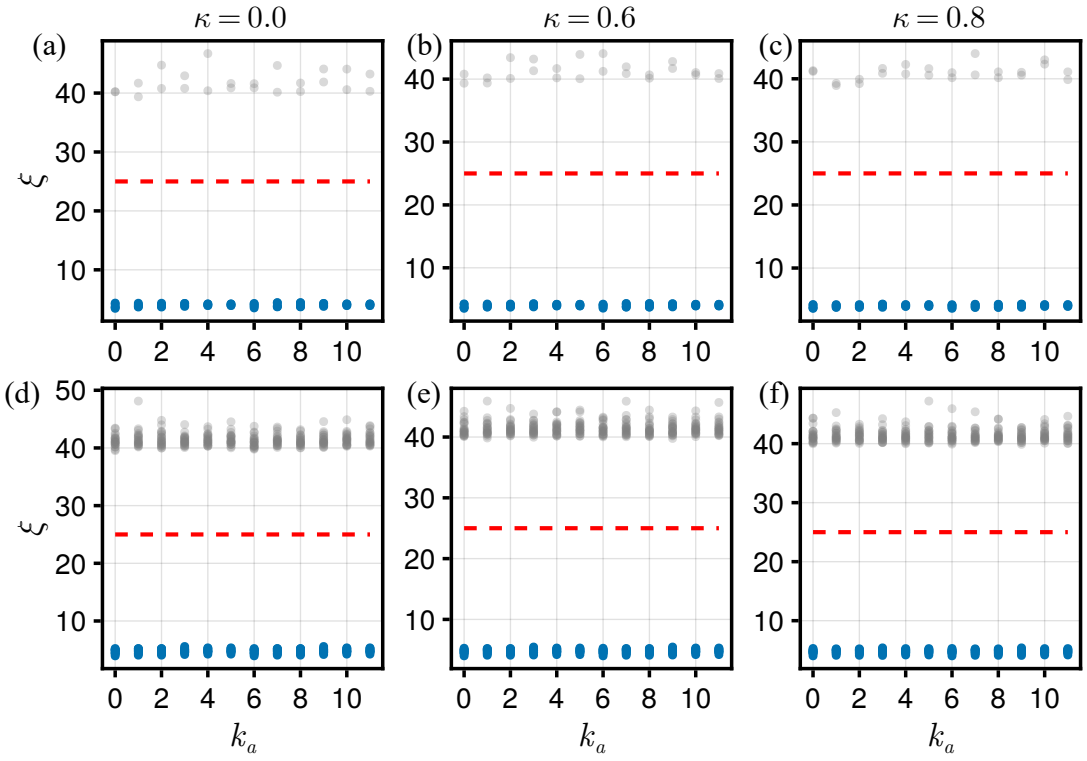

FIG. S7. Entanglement spectrum calculated using the right eigenvectors of the zero modes for $L_x = 6, L_y = 4, \phi = 1/2$. $n_A = 2$ for (a)-(c) and $n_A = 3$ for (d)-(f).

XI. SIMPLE INTERPRETATION OF NEGATIVE ENERGY STATES

In this section, we give a simple interpretation for why negative energy states in Fig. 3(d) in the main text can emerge under a positive definite interaction.

Our total interacting Hamiltonian is

$$H(\kappa) = H_0(\kappa) + \sum_j \frac{U}{2} a_j^\dagger a_j^\dagger a_j a_j, \tag{S57}$$

where the first term is the single-particle Kapit-Mueller model and the second is the interaction. According to Weyl inequality, the lowest eigenvalue of the sum of two Hermitian operators A and B, is greater than or equal to the sum of the lowest eigenvalues of A and B, i.e, $\lambda^{\min}_{A+B} \geq \lambda^{\min}_{A} + \lambda^{\min}_{B}$. Therefore, in the Hermitian limit, the FCIs, which minimize both the kinetic and interaction terms, are always the ground states.

On the other hand, Weyl equality is only in the Hermitian regime, and we can find a counterexample even when only one of the two operators is non-Hermitian and has real spectra. Given two simple 2×2 matrices:

$$A = \begin{pmatrix} -8 & -9 \\ 9 & 10 \end{pmatrix}, \quad B = \begin{pmatrix} 1 & 0 \\ 0 & 2 \end{pmatrix},$$

the eigenvalues of A are $\lambda_A = 1, 1$ and those of B are $\lambda_B = 1, 2$. Although eigenvalues of A and B are all positive, the eigenvalues of

$$S = A + B = \begin{pmatrix} -7 & -9 \\ 9 & 12 \end{pmatrix}$$

are $\lambda_S \approx 5.541, -0.541$, with a negative one. Therefore, minimizing kinetic energy and interaction ennergy, respectively, do not necessarily lead to the lowest total energy in the non-Hermitian regime. This explains why states in Fig. 3(b)(d) under large non-Hermiticity can counterintuitively acquire negative energy with a positive definite interaction, which is attributed to the distinct feature of non-Hermitian operators.

XII. SIGNATURES OF SUPERFLUID

In this section, we show evidence of superfluid for the negative energy states competing with FCIs by calculating the superfluid density.

We calculate the superfluid density by the second derivative of the many-body state energy with respect to the twisted boundary phase Φ_x (Φ_y) close to $\Phi_x = 0$ ($\Phi_y = 0$) [6, 7]

$$\rho_{s,y} = \frac{L_y}{L_x} \frac{\partial^2 E_M}{\partial \Phi_y^2}\Big|_{\Phi_y=0}, \tag{S58}$$

$$\rho_{s,x} = \frac{L_x}{L_y} \frac{\partial^2 E_M}{\partial \Phi_x^2}\Big|_{\Phi_x=0}, \tag{S59}$$

where $\rho_{s,x}$ and $\rho_{s,y}$ are superfluid density along x and y directions, respectively. We show $\rho_{s,x}$ and $\rho_{s,y}$ of the lowest energy state at $\kappa = 0.7$ and 0.75 in Fig. S8, for which the energy is negative. We see as the system size L_x and L_y increase, $\rho_{s,x}$ and $\rho_{s,y}$ grow in overall, implying the negative energy states host nonzero superfluid density.

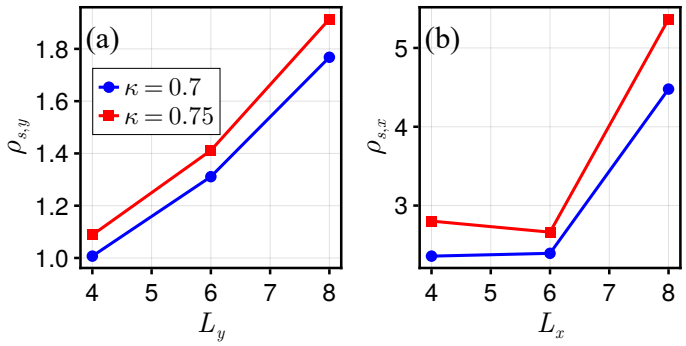

FIG. S8. Superfluid density (a) $\rho_{s,y}$ as a function of L_y for $L_x = 4$ and $\rho_{s,x}$ as a function of L_x for $L_y = 4$.

XIII. BEYOND THE SINGLE-BAND PROJECTION

In this section, we demonstrate the many-body energy spectrum under larger interaction strength without single-band projection.

We show the many-body energy spectrum without the single-band projection as a function of κ under $U = 1, 10$ and 100 in Fig. S9(a),(b) and (c), respectively. For all the cases, we see FCIs as the ground states below a critical κ and transitions into a regime with negative energy states for larger κ. $U = 100$ shows the physics in the hard-core limit, on the opposite side of the single-band projection. Therefore our finding is general for the whole range of interaction strength.

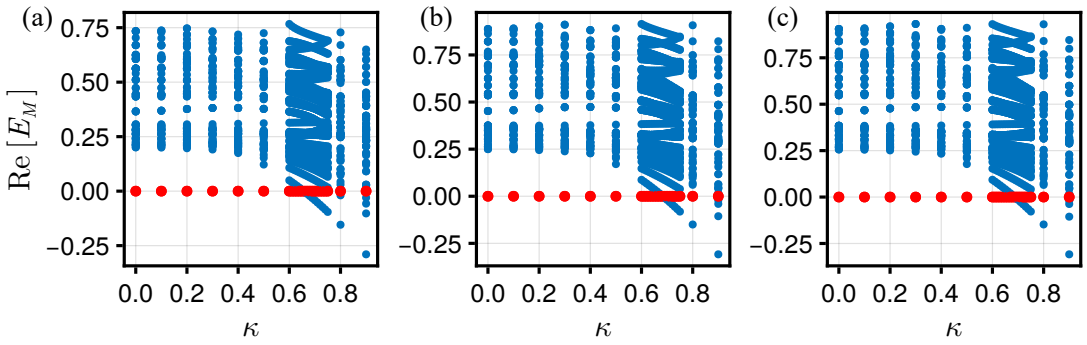

FIG. S9. Many-body energy spectrum without the single-band projection as a function of κ under (a) $U = 1$, (b)$U = 10$ and (c) $U = 100$ at $L_x = 4, L_y = 4, \phi = 1/2$.

To show $U = 100$ is in the hard-core limit, we compare the many-body energy spectrum of $U = 100$ and $U = 1000$ as shown in Fig. S10. We cannot tell the difference between (a) with $U = 100$ and (b) with $U = 1000$ at $\kappa = 0.6$ and similarly (c) and (d) at $\kappa = 0.9$, indicating $U = 100$ is large enough to show the physics of hard-core bosons.

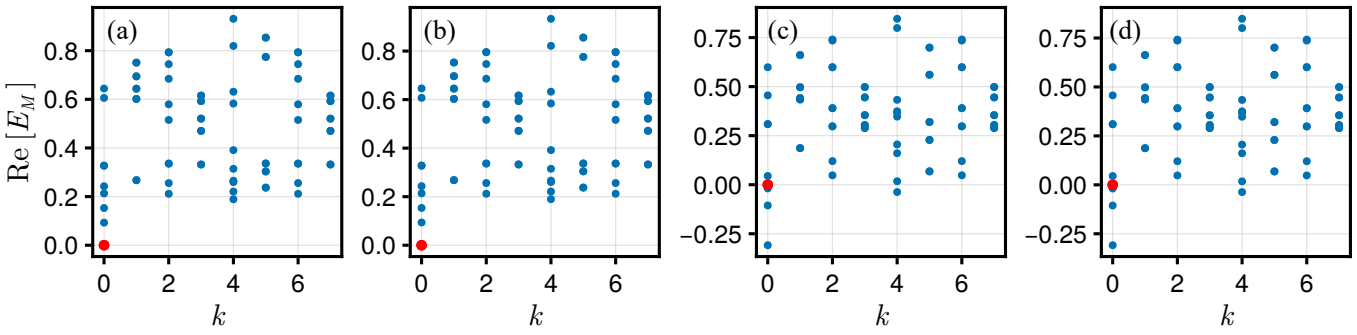

FIG. S10. Real part of the many-body energy spectrum at $L_x = L_y = 4, \phi = 1/2$. (a) $U = 100, \kappa = 0.6$, (b) $U = 1000, \kappa = 0.6$, (c) $U = 100, \kappa = 0.9$, (d) $U = 1000, \kappa = 0.9$.

XIV. ILLUSTRATION OF THE BREAKDOWN OF VARIATIONAL PRINCIPLE IN NON-HERMITIAN SYSTEMS

In this section, we will give a detailed explanation on the breakdown of the variational principle in non-Hermitian systems and its effect on the critical non-Hermiticity strength κ_c under different interacting strength.

Let us recall the variational principle in Hermitian quantum mechanics first. For a Hermitian Hamiltonian H acting on a Hilbert space $\mathcal{H}$, the expectation value $\langle\psi|H|\psi\rangle \geq E_G$ for any state $|\psi\rangle$ in $\mathcal{H}$ and E_G is the ground state energy of H, and the equality holds when $|\psi\rangle$ takes the ground state $|\psi_G\rangle$. Given a subspace $\mathcal{H}_1 \subseteq \mathcal{H}$, we can write the matrix representation of the Hamiltonian H as

$$H = \begin{pmatrix} H_1 & H_{12} \\ H_{21} & H_2 \end{pmatrix},$$

where H_1, H_2, H_{12}, H_{21} are matrices and H_1 is the matrix representation in subspace $\mathcal{H}_1$. The variational principle can be formulated as $E_1 \geq E_G$ with E_1 being the lowest eigenvalue of H_1, because $E_1 = \langle\psi_1|H|\psi_1\rangle \geq E_G$ with the eigenvector $|\psi_1\rangle$ of H_1 being a vector in both $\mathcal{H}_1$ and $\mathcal{H}$.

In our interacting model, as shown in Fig. 3(d) in the main text, the lowest real part of the energy of the states other than the zero-energy FCIs decreases as the non-Hermiticity strength κ increases, and drops to below zero after a critical value. The single-band projection corresponds to the variation within a sub Hilbert space, thus the lowest eigenenergy under projection cannot be lower than the ground state energy obtained by diagonalizing the complete Hamiltonian without single-band projection, i.e., $E_G^{\mathrm{Proj}}(\kappa) \geq E_G^{\mathrm{Full}}(\kappa)$, if the variational principle still applies. If that is the case, by diagonalizing the complete Hamiltonian, the lowest real part of the energy other than the zero modes would be zero or negative at the critical value under the single-band projection $\kappa_{c,s}$, i.e., $E_G^{\mathrm{Proj}}(\kappa_{c,s}) \geq E_G^{\mathrm{Full}}(\kappa_{c,s})$. Therefore, as $E_G(\kappa_1) \geq E_G(\kappa_2)$ for $\kappa_1 \leq \kappa_2$ obtained by numerics, the critical value for the full interacting model $\kappa_{c,f}$ is not larger than $\kappa_{c,s}$. However, our numerics demonstrate that κ_c increases as we discard the single-band projection, evidencing the breakdown of the variational principle in non-Hermitian systems.

We show the breakdown by an example of a 2×2 matrix:

$$H = \begin{pmatrix} 0 & -1 \\ 1 & 2 \end{pmatrix},$$

where $H_1 = 0$ can be considered as the matrix representation in a restricted Hilbert space of one dimension, with lowest eigenvalue $E_1 = 0$. The eigenvalues of H are $1, 1$, i.e., $E_G = 1$, obviously violating the variational principle $E_1 \geq E_G$.

XV. $\phi = 1/3$ CASE

In this section, we show numerical results at flux $\phi = 1/3$ to illuminate the generality of our findings.

In Fig. S11, we show the complex energy of the non-Hermitian KM model in Eq. 1 of the main text with $\kappa = 0, 1, 1.4, 2$ from left to right. The same as the $\phi = 1/2$ case, we see the flat band also remains exactly real and flat under the non-Hermitian deformation. The flat band energy is pinned at $E = -1$ and the loop formed by excited states enlarges as κ increases. After the gap closing, the flat band tunnels into the loop while remain intact.

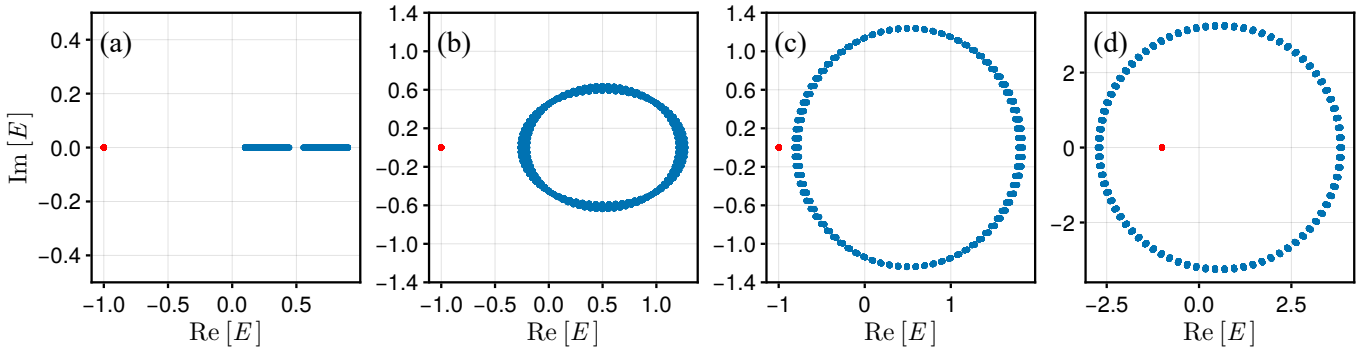

FIG. S11. Single-particle energy in the complex energy plane of the non-Hermitian KM model at $\phi = 1/3$ for (a) $\kappa = 0$ (b) $\kappa = 1$ (c) $\kappa = 1.4$ (d) $\kappa = 2$.

The real and imaginary parts of the quantum geometry at $\phi = 1/3$ are shown in Fig. S12(a) and (b), respectively. The quantum geometry at $\phi = 1/3$ also satisfies the generalized ideal condition in Eq. (7)(8) in the main text.

In Fig. S13, we show the real part of the many-body energy spectrum at $\kappa = 0.0, 0.7$ and 0.8 in (a), (b) and (c), respectively. We see zero-energy modes as the ground states at $\kappa = 0.7$, while at $\kappa = 0.8$, negative energy states emerge. The transition is shown in Fig. S13(c) by the energy spectrum as a function of κ.

XVI. DISSIPATIVE OPEN QUANTUM SYSTEMS

In this section, we show how to realize the non-Hermitian FCIs in dissipative open quantum systems based on the Lindblad master equation and estimate the lifetime accordingly.

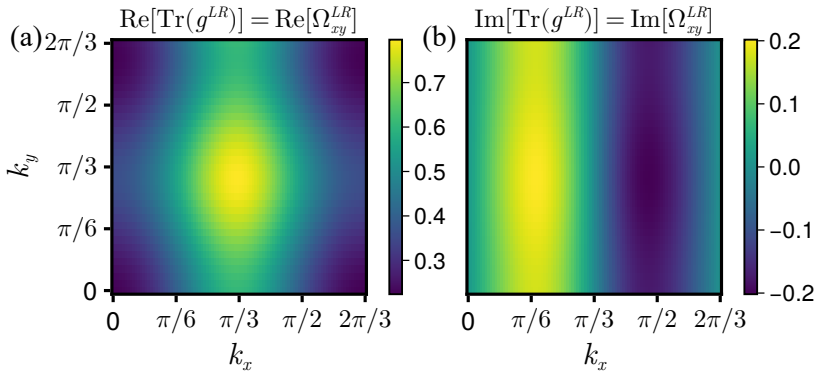

FIG. S12. (a) Real and (b) imaginary part of the quantum geometry at $\phi = 1/3$ of one-third of the magnetic Brillouin zone.

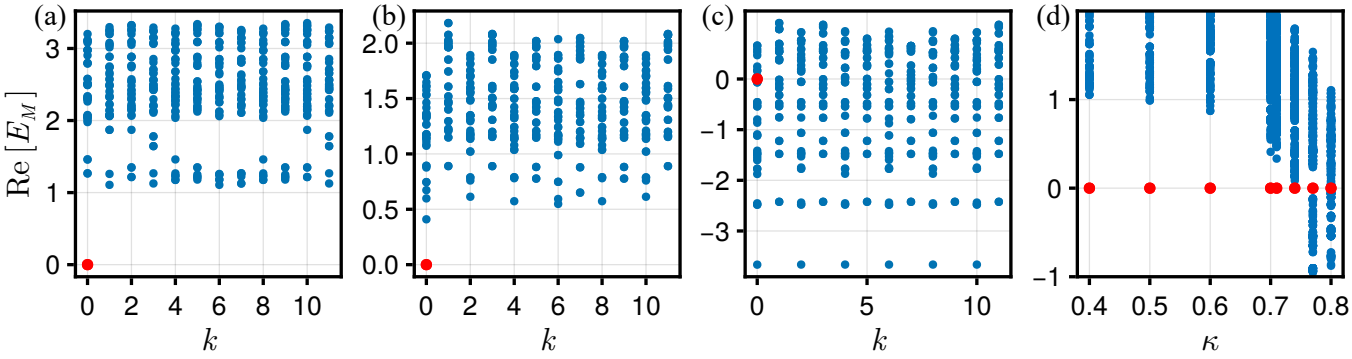

FIG. S13. Real part of the many-body energy spectrum for $L_x = 6, L_y = 6, \phi = 1/3$: (a) $\kappa = 0$ (b) $\kappa = 0.7$ (c) $\kappa = 0.8$ (d) with respect to κ.

We consider an open quantum system described by the Lindblad master equation:

$$\frac{\mathrm{d}\rho}{\mathrm{d}t} = -i[H_{KM}, \rho] + \sum_{i<j}(2L_{ij}\rho L_{ij}^\dagger - \{L_{ij}^\dagger L_{ij}, \rho\}) \tag{S60}$$

$$= -i(H_{\text{eff}}\rho - \rho H_{\text{eff}}^\dagger) + \sum_{i<j} 2L_{ij}\rho L_{ij}^\dagger, \tag{S61}$$

where $H_{KM} = \sum_{i\neq j} J_{ij} a_i^\dagger a_j$ is the Hermitian Hamiltonian of the pristine KM model with J_{ij} defined in the main text, the Lindblad operator $L_{ij} = A_{ij}a_i - iB_{ij}a_j$ characterizes the dissipation and the effective non-Hermitian Hamiltonian $H_{\text{eff}} = H_{KM} - i\sum_{i<j} L_{ij}^\dagger L_{ij}$. As $L_{ij}^\dagger L_{ij} = |A_{ij}|^2 a_i^\dagger a_i + |B_{ij}|^2 a_j^\dagger a_j + iB_{ij}^* A_{ij} a_j^\dagger a_i - iA_{ij}^* B_{ij} a_i^\dagger a_j$, if we choose $A_{ij}^* B_{ij} = \gamma(x_i - x_j)J_{ij}$, we have

$$H_{\text{eff}} = \sum_{i<j} J_{ij}[1 - \gamma(x_j - x_i)]a_i^\dagger a_j + J_{ij}^*[1 - \gamma(x_i - x_j)]a_j^\dagger a_i - i\Delta_i a_i^\dagger a_i \tag{S62}$$

with $\Delta_i = \sum_{i<j} |A_{ij}|^2 + \sum_{j<i} |B_{ji}|^2$. For $\gamma = \kappa(\pi/2)(1-\phi)$, H_{eff} is equivalent to the non-Hermitian KM model Eq. (1) in the main text to the first order of γ except for the loss term $-i\Delta_i a_i^\dagger a_i$. By setting $A_{ij} = \sqrt{\gamma|(x_i - x_j)J_{ij}|}, B_{ij} = \gamma(x_i - x_j)J_{ij}/\sqrt{\gamma|(x_i - x_j)J_{ij}|}$, we see Δ_i is constant on a torus due to the translational symmetry and approximately constant in the bulk under OBCs as Δ_i is dominated by the nearest few sites around site i due to the exponential decay of J_{ij}. Therefore, the effect of the loss term $-i\Delta_i a_i^\dagger a_i$ in H_{eff} can be accounted for as a constant shift of each eigenenergy by an imaginary value $-i\Delta n_b$ with $\Delta = \Delta_i$ and n_b being the number of particles.

For open quantum systems, we concern about the eigensystem of the Liouvillian operator $\mathcal{L}$ in the Lindblad master equation $\mathrm{d}\rho/\mathrm{d}t = \mathcal{L}\rho$, that is, $\mathcal{L}\rho = \lambda\rho$, with $\mathrm{Re}[\lambda] < 0$ corresponding to the dissipative case associated with lifetime $\tau \sim 1/\mathrm{Re}[-\lambda]$. The explicit form of $\mathcal{L}$ can be found in Eq. S60. It is proved [8] that in the presence of loss only or gain only, the eigenstate is

$$\rho_{jk} = |\psi_j^R\rangle\langle\psi_k^R| \tag{S63}$$

with eigenvalue $\lambda_{jk} = -i(E_j - E_k^*) = \mathrm{Im}(E_j) + \mathrm{Im}(E_k)$, where $|\psi_j^R\rangle$ is the right eigenvector of H_{eff} with eigenenergy E_j. For the pure state of non-Hermitian Laughlin states, i.e., $\rho_{Lau} = |\psi_{Lau}^R\rangle\langle\psi_{Lau}^R|$, the corresponding eigenvalue is $\lambda_{Lau} = 2\mathrm{Im}(E_{Lau})$. In the main text, the energy of the non-Hermitian Laughlin state is purely real and exactly zero. For the effective Hamiltonian arising from the dissipative Lindblad master equation, due to the extra loss term, $E_{Lau} = -i\Delta n_b$, and the eigenvalue of the Liouvillian operator is $\lambda_{Lau} = -2\Delta n_b$, corresponding to the lifetime $\tau \sim 1/(2\Delta n_b)$. Note that due to the loss, the steady state is the vacuum.

In Sec. VIII, we have shown that by taking a complex interaction $U = |U|e^{i\theta}$, we can render the non-Hermitian FCIs the only states with zero imaginary part of the energy while all the other states with nonzero negative imaginary part. The imaginary interaction can be realized by two body loss, i.e., the Lindblad operator $L_i \sim a_i a_i$. In this case, taking into account the imaginary energy shift $i\Delta n_b$, the energy of FCIs has the smallest absolute value for the imaginary part. Subsequently, the Laughlin state ρ_{Lau} has the smallest absolute value for the imaginary part of the Liouvillian eigenvalue λ, corresponding to the longest lifetime in the specific particle number sector.

[1] F. D. M. Haldane and E. H. Rezayi, Periodic laughlin-jastrow wave functions for the fractional quantized hall effect, Phys. Rev. B **31**, 2529 (1985).

[2] E. Kapit and E. Mueller, Exact parent Hamiltonian for the quantum Hall states in a lattice, Phys. Rev. Lett. **105**, 215303 (2010).

[3] T. Yoshida, K. Kudo, and Y. Hatsugai, Non-hermitian fractional quantum hall states, Sci. Rep. **9**, 16895 (2019).

[4] N. Regnault and B. A. Bernevig, Fractional Chern insulator, Phys. Rev. X **1**, 021014 (2011).

[5] B. A. Bernevig and F. D. M. Haldane, Model fractional quantum hall states and jack polynomials, Phys. Rev. Lett. **100**, 10.1103/PhysRevLett.100.246802 (2008).

[6] M. E. Fisher, M. N. Barber, and D. Jasnow, Helicity modulus, superfluidity, and scaling in isotropic systems, Phys. Rev. A **8**, 1111 (1973).

[7] A. Paramekanti, N. Trivedi, and M. Randeria, Upper bounds on the superfluid stiffness of disordered systems, Phys. Rev. B **57**, 11639 (1998).

[8] J. M. Torres, Closed-form solution of lindblad master equations without gain, Phys. Rev. A **89**, 052133 (2014).